1 **Retrieval and analysis of the composition of an aerosol mixture through Mie-Raman-**

2 **Fluorescence lidar observations.**

4 Igor Veselovskii[1], Boris Barchunov[1], Qiaoyun Hu[2], Philippe Goloub[2], Thierry Podvin[2], Mikhail

5 Korenskii[1], G. Dubois[2], William Boissiere[2], Nikita Kasianik[1]

7 *[1]Prokhorov General Physics Institute of the Russian Academy of Sciences, Moscow, Russia.*

8 *[2]Univ. Lille, CNRS, UMR 8518 - LOA - Laboratoire d'Optique Atmosphérique, F-59650 Lille,*

9 *France*

10 **Correspondence**: Philippe Goloub (philippe.goloub@univ-lille.fr)

12 **Abstract**

13 In the atmosphere, aerosols can originate from numerous sources, leading to the mixing of different

14 particle types. This paper introduces an approach to the partitioning of aerosol mixtures in terms

15 of backscattering coefficients. The method utilizes data collected from the Mie-Raman-

16 fluorescence lidar, with the primary input information being the aerosol backscattering coefficient

17 (β), particle depolarization ratio (δ), and fluorescence capacity (G_F). The fluorescence capacity is

18 defined as the ratio of the fluorescence backscattering coefficient to the particle backscattering

19 coefficient at the laser wavelength. By solving a system of equations that model these three

20 properties $(\beta, \delta$ and $G_F)$, it is possible to characterize a three-component aerosol mixture.

21 Specifically, the paper assesses the contributions of smoke, urban, and dust aerosols to the overall

22 backscattering coefficient at 532 nm. It is important to note that aerosol properties $(\delta$ and $G_F)$ may

23 exhibit variations even within a specified aerosol type. To estimate the associated uncertainty, we

24 employ the Monte Carlo technique, which assumes that G_F and δ are random values uniformly

25 distributed within predefined intervals. In each Monte Carlo run, a solution is obtained. Rather

26 than relying on a singular solution, an average is computed across the whole set of solutions, and

27 their dispersion serves as a metric for method uncertainty. This methodology was tested using

28 observations conducted at the ATOLL observatory, Laboratoire d'Optique Atmosphérique,

29 University of Lille, France.

31   **1. Introduction**

Studying the physicochemical properties of atmospheric aerosols is crucial for understanding their impact on Earth's radiation balance and climate. To simplify the complexity of aerosol composition, it is essential to classify aerosol types. Categorization of aerosols into several basic types, e.g. urban, dust, marine, biomass burning (Dubovik et al., 2002), allows to cover the range of variability of observed aerosol parameters and facilitates the analysis and interpretation of aerosol data. The multiwavelength Mie-Raman and HSRL (High Spectral Resolution Lidar) lidar systems provide an unique opportunity to derive height-resolved particle intensive properties, such as Angstrom exponents, lidar ratios, and depolarization ratios at multiple wavelengths. These properties can be used as inputs for classification schemes (Burton et al., 2012, 2013; Groß et al., 2013; Mamouri et al., 2017; Papagiannopoulos et al., 2018; Nicolae et al., 2018; Hara et al., 2018; Voudouri et al., 2019; Wang et al., 2021; Mylonaki et al., 2021; Wandinger et al., 2023; Floutsi et al., 2023b). However, aerosols in the atmosphere often originate from multiple sources, leading to the mixing of different particle types. To understand the impact of different aerosol types within a mixture, it is necessary to quantify the content of each type.

In the cases involving mixtures of two aerosol types with significantly different depolarization ratios, the partitioning of aerosol backscattering coefficients becomes straightforward (Sugimoto and Lee, 2006; Tesche et al., 2009; Miffre et al., 2020). Burton et al. (2014) have formulated the mixing rules for several aerosol intensive parameters, such as lidar ratio, backscatter color ratio, depolarization ratio, and applied these rules to two-component aerosol mixtures. However, the partition becomes increasingly challenging when dealing with more than two types of particles. The limited number of lidar-measured intensive particle properties specific to individual aerosol types contributes to this challenge. Even for a single aerosol type, the measured particle parameters, such as lidar ratios, demonstrate a wide range of variability (Floutsi et al., 2023a). Distinguishing between urban and smoke particles poses a particular challenge as these two types exhibit similar lidar-measured properties (Floutsi et al., 2023a). Therefore, additional independent information is needed to enhance the characterization of aerosol parameters.

Independent information about aerosol properties can be obtained through fluorescence lidar measurements (Reichardt et al., 2018, 2023; Veselovskii et al., 2020; Zhang et al., 2021). The fluorescence lidar allows evaluating the fluorescence backscattering coefficient β_F, which is derived from the ratio of fluorescence and nitrogen Raman backscatters (Veselovskii et al., 2020).

The particle intensive property in fluorescence lidar measurements is the fluorescence capacity G_F, which is the ratio of β_F to the aerosol backscattering coefficient at the laser wavelength. The fluorescence capacity of smoke is approximately one order higher than that of urban particles, providing a basis for distinguishing between these two aerosol types (Veselovskii et al., 2022). Additionally, recent studies have shown that a classification scheme relying on two intensive parameters - the particle depolarization ratio at 532 nm (δ_{532}) and the fluorescence capacity, effectively separates four aerosol types: dust, smoke, pollen, and urban, as demonstrated in the publication of Veselovskii et al. (2022). It is noteworthy that the classification scheme in that paper does not discriminate particles based on their absorption properties, so the "urban" type encompasses both continental aerosol and anthropogenic pollution. Furthermore, maritime aerosol is not included in the classification at present, as the lidar observations were performed over Lille, where maritime particles are not prevalent (though the possibility of its inclusion is acknowledged).

The algorithm presented in the study of Veselovskii et al. (2022) showcases the capability to perform aerosol classification with high spatiotemporal resolution. However, as mentioned earlier, it is essential to quantify the content of the mixture. In this study, we extended the approach beyond classification to partition aerosol mixtures in terms of the backscattering coefficients of basic aerosol types. To test the algorithm, we analyzed observations at the ATOLL (ATmospheric Observation at liLLe) at Laboratoire d'Optique Atmosphérique, University of Lille, between 2020 and 2023, performed during periods of strong smoke and dust episodes. We begin by providing a description of the lidar system (Section 2.1) and in Section 2.2, a novel approach for mixture partition is presented. In the results section (Section 3), we present three case studies that demonstrate how the algorithm operates. The paper concludes with a summary of our findings in the conclusion section.

2. Experimental setup and approach to aerosol mixture partition

2.1. Lidar system.

The Mie-Raman-fluorescence lidar LILAS (LIlle Lidar AtmosphereS) is equipped with a tripled Nd:YAG laser that operates at a repetition rate of 20 Hz and has a pulse energy of approximately 100 mJ at 355 nm. A 40 cm aperture Newtonian telescope is utilized to collect the backscattered light, and Licel transient recorders with a range resolution of 7.5 m are employed to

94   digitize the lidar signals. This configuration allows for simultaneous detection in both analog and
95   photon counting modes. The objective of the LILAS system is to detect elastic and Raman
96   backscattering, which enables the measurement of various properties through the 3β+2α+3δ data
97   configuration. This includes three particle backscattering coefficients $(\beta_{355}, \beta_{532}, \beta_{1064})$, two
98   extinction coefficients $(\alpha_{355}, \alpha_{532})$, and three particle depolarization ratios $(\delta_{355}, \delta_{532}, \delta_{1064})$. The
99   particle depolarization ratio, determined as a ratio of cross- and co-polarized components of the
100 particle backscattering coefficient, was calculated and calibrated in the same way as described in
101 Freudenthaler et al. (2009). Additionally, the LILAS system is capable of profiling the laser-
102 induced fluorescence of aerosol particles. This is achieved by using a wideband interference filter
103 with a width of 44 nm, centered at 466 nm, as suggested by Veselovskii et al. (2020). Due to the
104 strong sunlight background during daytime, the fluorescence observations are limited to nighttime
105 hours.

106   The calculation of the fluorescence capacity G_F can be performed using backscattering
107 coefficients at any laser wavelength. In our study, we specifically used β_{532}, as it is determined
108 using rotational Raman scattering and is considered to be the most reliable, thus $G_F = \dfrac{\beta_F}{\beta_{532}}$. To
109 supplement our measurements, additional information about atmospheric properties was obtained
110 from radiosonde measurements conducted at Herstmonceux (UK) and Beauvechain (Belgium)
111 stations, which are located approximately 160 km and 80 km away from the observation site,
112 respectively. The lidar measurements were primarily conducted vertically. In cases where
113 observations were made at an angle to the horizon, the corresponding information has been
114 included in the captions of the figures.
115

116   **2.2. Approach for the mixture partition**
117   The lidar system measures up to nine independent properties of aerosols. However, our
118 main focus is on separation the backscatters of individual aerosol types with high spatiotemporal
119 resolution. To calculate parameters related to the extinction coefficient, such as lidar ratio or
120 extinction Angstrom exponent, it is necessary to average lidar profiles over a substantial
121 spatiotemporal interval. In this study, as a first step, we use three parameters with high resolution
122 in both height and temporal domains: the backscattering coefficient β_{532}, the depolarization ratio
123 δ_{532} and the fluorescence capacity G_F. Moreover, the calculation process partially cancels out the

124 overlap functions, allowing us to derive β_{532}, δ_{532} and G_F closer to the ground compared to aerosol

125 extinction. We are considering a scenario where only three externally mixed aerosol types occur,

126 such as smoke (s), dust (d), and urban (u). The aerosol and fluorescence backscattering coefficients

127 (β_{532} and β_F) are the sum of their respective contributions.

128 $\beta_{532} = \beta_{532}^s + \beta_{532}^d + \beta_{532}^u$ (1)

129 $\beta_F = \beta_F^s + \beta_F^d + \beta_F^u$ (2)

130 The fluorescence capacities for each aerosol type are:

131 $G_F^i = \dfrac{\beta_F^i}{\beta_{532}^i}$ (3)

132 where $i = s, d, u$. The fractions of β_{532} for individual aerosol types are:

133 $\eta_i = \dfrac{\beta_{532}^i}{\beta_{532}}$. (4)

134 By definition:

135 $\eta_s + \eta_d + \eta_u = 1$. (5)

136 The fluorescence capacity can be expressed as a linear combination of the fluorescence

137 capacities of each aerosol type, as shown in Eq. 6:

138 $G_F = \eta_s G_F^s + \eta_d G_F^d + \eta_u G_F^u$ (6)

139 The particle depolarization ratio is a ratio of the cross- and co-polarized component of the

140 backscattering coefficient: $\delta_{532} = \dfrac{\beta_{532}^{\perp}}{\beta_{532}^{\parallel}}$. However, for the mixture analysis, the use of the

141 depolarization potential $\delta_{532}' = \dfrac{\delta_{532}}{1 + \delta_{532}}$ is preferable, because δ', the same as G_F, is a linear

142 combination of the depolarization potentials of individual particle types ($\delta_{532}'^s, \delta_{532}'^d, \delta_{532}'^u$), as outlined

143 by Burton et al. (2014).

144 $\delta_{532}' = \eta_s \delta_{532}'^s + \eta_d \delta_{532}'^d + \eta_u \delta_{532}'^u$ (7)

145 Finally, we have a system of three equations (5-7) from which we can determine the relative

146 contributions of each aerosol type by finding η_s, η_d and η_u. In our study, we solve the system (Eq.

147 5-7) using the least squares method with an additional constraint on the non-negativity of solutions.

148 As mentioned earlier, the particle parameters may vary within predetermined ranges, even for a

149 specific aerosol type. However, the exact values of G_F^i and $\delta_{532}^{'}$ at a specific height/time pixel are

150 unknown. To address the uncertainty in η_i, we employ the Monte Carlo technique, assuming that

151 G_F^i and $\delta_{532}^{'}$ are random values uniformly distributed within the predetermined intervals. For each

152 Monte Carlo trial, random values of G_F^i and $\delta_{532}^{'}$ are generated. Instead of relying on a single

153 solution, we conduct a series of Monte Carlo trials in order to obtain a set of solutions and calculate

154 the average of this set. The dispersion of these solutions is taken as a measure of method

155 uncertainty. The number of Monte Carlo trials was set to 100 and further increase in this number

156 did not significantly impact either the final average or the dispersion of solutions. In our

157 classification scheme, we include four types of aerosols (smoke, pollen, urban, dust). Nevertheless,

158 the system of equations (Eq. 5-7) consists of only three equations. Given that it is highly unlikely

159 to have all four aerosol types coexisting at a single height/time pixel, one of the four types can be

160 excluded a priori based on a G_F-δ_{532} diagram or other pertinent considerations. Another option is

161 to exclude one aerosol type at each height/time pixel based on the lidar data itself, as described

162 below. Such method we will call Automatic Type Selection (ATS)

163   For ATS, we solve the system Eq. 5-7 for the triplets (*S, P, U*), (*S, P, D*), (*S, D, U*), and (*P,*

164 *D, U*), where *S, D, U, P* denote Smoke, Dust, Urban, Pollen, respectively. To determine which

165 aerosol types can be excluded, we use the discrepancy for Eq. 6 and 7 as a criterion. Specifically,

166 we calculate the difference between the input data (G_F-δ_{532}) and the corresponding values obtained

167 by substituting the solution into the right-hand side of Eq. 6 and 7. The aerosol triplet that provides

168 the least discrepancy is chosen for this single Monte Carlo trial and for the height/time pixel. This

169 procedure is repeated for every Monte Carlo trial, and after averaging, the spatiotemporal

170 distributions of η_s, η_p, η_u, and η_d are evaluated.

171

172 **3. Application of partition algorithm to lidar observations**

173   **3.1. Range of particle parameters used in inversion scheme.**

174   The uncertainty of the partitioning of backscattering coefficients depends on the range of

175 G_F and δ_{532} variations in each aerosol type. To establish this range, we analyzed measurement

176 sessions at the ATOLL for the period of 2020-2023. Our focus was on observation episodes

177 characterized by stable atmospheric conditions, where only a single aerosol type predominated, at

178 least within specific height/time intervals. Moreover, we took precautions to ensure that the

179 relative humidity in the selected intervals remained below 60% to minimize the impact of particle

180 hygroscopic growth. The example of such impact is presented in Fig.6 of Veselovskii et al. (2024).

181 Based on the obtained results, we summarized the ranges of parameter variation in Table 1. The

182 ranges are slightly different from the ones in Table 1 of Veselovskii et al. (2022), because since

183 that publication numerous observations were performed, providing more material for analysis. The

184 depolarization ratios δ_{532} for smoke and urban particles fall within the range of 2%-8%, while for

185 dust, this range is 25%-35%. The depolarization ratio of long transported dust can be lower, but at

186 this stage, we do not consider possible modifications of dust properties during transportation. We

187 attribute lower values of δ_{532} to the mixing of dust with pollutants (urban aerosol in our model).

188 Should be mentioned, that depolarization ratio of smoke in the upper troposphere can be as high

189 as 20% (Ohneiser et al., 2020), however, in the low and middle troposphere, where partitioning

190 was performed, we limited δ_{532} by the value of 8%.

191   The fluorescence capacity of smoke is high, due to the presence of organic carbon. In the

192 upper troposphere G_F can reach 10×10^{-4} (Veselovskii et al., 2024), but below 8 km, it mainly falls

193 within the range of $(2.5\text{-}4.5)\times10^{-4}$. For dust and urban particles, the values of fluorescence

194 capacities are within the intervals of $(0.05\text{-}0.45)\times10^{-4}$ and $(0.2\text{-}0.8)\times10^{-4}$, respectively.

195 Determining the ranges of δ_{532} and G_F for pollen is particularly challenging because, in the north

196 of France, pollen is commonly mixed with other aerosol types. Moreover, the depolarization of

197 pollen particles varies significantly from one type to another (Cao et al., 2010). In the Lille area,

198 one dominant taxon is birch (Veselovskii et al., 2021) with a depolarization ratio of δ_{532} at around

199 30% (Cholleton et al., 2022). In our analysis, the depolarization ratio is set within the 30%-40%

200 interval. The pollen consist of biological materials and their fluorescence capacity is higher than

201 that of urban particles. From our measurements the variation range of G_F for pollen is estimated

202 to be within $(1.0\text{-}2.5)\times10^{-4}$.

203

204 Table 1. Variation ranges of fluorescence capacity and the particle depolarization ratio for different

205 types of aerosols.

Type	G_F, 10^{-4}	δ_{532}, %
Smoke	2.5÷4.5	2.0÷8
Pollen	1÷2.5	30÷40

Urban	0.2÷0.8	2.0÷8
Dust	0.05÷0.45	25÷35

206

207 Below, we present three examples of applying the described approach to measurements performed
208 at the ATOLL observatory.

209

210 **3.2. Episode on March 27-28, 2022. Three types of particles are observed within different**
211 **spatiotemporal domains.**

212 The spatiotemporal distributions of the aerosol backscattering coefficient β_{532}, the particle
213 depolarization ratio δ_{532}, and the fluorescence capacity G_F on March 27-28, 2022, are shown in
214 Fig.1. Relative humidity decreased with height, ranging from 70% at 600 m to 55% at 1800 m.
215 Aerosols were primarily found below 2500 m, with several distinguishable particle types identified.
216 The particle depolarization ratio increased to 30% at 2000 m during the 20:00-22:00 UTC period,
217 indicating the presence of dust. Additionally, high values of the fluorescence capacity (up to
218 2.5×10^{-4}) for the 00:00-05:00 UTC period suggest the presence of smoke.

219 Fig.2a presents the G_F-δ_{532} diagram for these measurements (Veselovskii et al., 2022). The
220 red boxes represent the parameter ranges used for aerosol classification, which are slightly broader
221 than those outlined in Table 1 to account for mixtures where one type is predominant. Dust, smoke,
222 and urban particles can be distinguished on the diagram, together with intervals indicating mixed
223 particle types. Although March is typically a pollen season in Lille, pollen particles did not
224 significantly contribute to the observed episode. Utilizing this classification scheme, we assess the
225 spatiotemporal distribution of aerosol types in Fig.2b, following the methodology outlined in
226 Veselovskii et al. (2022). Regions predominated by dust, smoke, and urban particles are clearly
227 identified. A small amount of pollen is observed towards the end of the session at approximately
228 700 m height. The grey color in Fig.2b represents aerosol mixtures where the particle type cannot
229 be definitively identified. The aerosol classification presented in Fig. 2b finds support in the results
230 of the HYSPLIT Backward Trajectory Analysis (Stein et al., 2015) depicted in Figure 3.
231 Specifically, the air masses below 1000 m height were transported over the Belgium, and the
232 presence of urban aerosol is expected. Conversely, the air masses above 1500 m were transported
233 over regions with extensive forest fires in Greece, suggesting a potential mixture of smoke and
234 dust.

235   By applying the partition technique described in Sect.2.2, we can determine the contribution
236   of each particle type to the total backscattering coefficient β_{532}. The spatiotemporal distributions of
237   η_s, η_u, and η_d in Fig.4 were assessed assuming that pollen contribution can be neglected. The
238   algorithm operates smoothly, showing distributions without any unrealistic high-frequency
239   oscillations. By observing the distributions, it can be concluded that the smoke plume actually
240   contains a significant amount of urban aerosol, while the dust plume does not show the presence
241   of other particle types.

242   The distributions in Fig.4 represent the mean values of η_s, η_u, and η_d. To understand the
243   uncertainty caused by potential variations in particle characteristics, Fig.5 displays the vertical
244   profiles of η_s, η_u, and η_d for the period between 21:00-22:00 UTC, along with the corresponding
245   standard deviations. Urban particles are predominant below 1000 m with a deviation from the
246   mean value of roughly 5%. Above 1500 m, η_u decreases to 0.05 and the uncertainty increases to
247   100%. Conversely, dust can be disregarded below 1000 m, but becomes predominant above 1000
248   m. Smoke contribution during the considered time period is low and only becomes noticeable
249   ($\eta_s \sim 0.15$) in the 1250-1500 m range. As mentioned earlier, the results in Fig. 4 were obtained
250   without considering pollen. To assess the potential impact of pollen on the results, the partition
251   was carried out for four aerosol types using the ATS approach, as described in Section 2.2. The
252   corresponding profiles of $\eta_{s,4}$, $\eta_{u,4}$, and $\eta_{d,4}$, are depicted in Fig.5 with magenta lines. Notably, the
253   profiles obtained for three and four aerosol types are similar. Pollen does have some effect on
254   smoke contribution (η_s decreased from 0.14 to 0.1), but its influence on dust and urban particle
255   contribution is negligible.

256

257   **3.3. Episode on October 1-2, 2023. Different types of aerosol form the layer structure.**
258   Observations at ATOLL in 2023 were notable for frequent intensive smoke events. North
259   American wildfire smoke, transported over the Atlantic, was observed from mid-May until
260   October. In some autumn episodes, smoke descended from the troposphere to ground level. One
261   such episode is shown in Fig.6, which presents the spatiotemporal distributions of β_{532}, δ_{532}, and
262   G_F during the night of October 1-2, 2023. During this period, the relative humidity decreased with
263   height, from 50% at 500 m to 30% at 3500 m. Strong aerosol layers were observed up to 5 km in
264   height, and the depolarization ratio δ_{532} exceeded 25% above 2000 m, indicating the predominance
265   of dust. However, below 1000 m, a low depolarization ratio ($\delta_{532} < 8\%$) was accompanied by a

266 high fluorescence capacity of particles (up to 3.0×10^{-4}), identifying them as smoke. The G_F-δ_{532}

267 diagram in Fig.7a highlights the pixels attributed to dust, smoke, and urban particles. There are

268 also intervals where these types were mixed. These regions with mixed aerosols are represented

269 by the grey color in the distribution of particle types in Fig.7b. The results of aerosol classification

270 agree with HYSPLIT backward trajectories analysis. Fig.8 shows the five-days back trajectories

271 over Lille on October 2, 2023, at 00:00 UTC. The air masses over the Atlantic, containing North

272 American smoke, descend from 5000 m to the ground, leading to the predominance of smoke over

273 Lille at 500 m. The air masses at 1500 m are transported over the continent and may contain

274 pollutants, whereas the air masses at 2700 m arrive from Africa and are loaded with dust. Fig. 9

275 depicts the spatiotemporal distributions of η_s, η_u, η_d, derived in assumption that only three aerosol

276 types occur. Urban aerosol is localized primarily between the smoke and dust layers. Vertical

277 profiles of η_s, η_u, η_d for the 22:00-23:00 UTC period are presented in Fig.10. Smoke predominates

278 below 1000 m, with a smoke contribution (η_s=0.7 at 750 m) evaluated with an uncertainty of about

279 20%. The contribution of urban particles within the smoke layer (at 750 m) is η_u=0.3, with a

280 corresponding uncertainty of approximately 30%. Dust predominates above 2000 m (η_d=0.8), and

281 the uncertainty of η_d estimation is below 15%. Although the existence of pollen in October is quite

282 improbable, for testing purposes, we performed an inversion for four aerosol types using the ATS

283 method (magenta lines in Fig.10). The impact of including pollen is most pronounced for dust at

284 1750 m, where η_d is about 25% decreased. However, the values obtained still fall within the

285 estimated range of uncertainty. From the examples considered, we conclude that the contributions

286 of three aerosol components to the backscattering coefficient can be determined through joint

287 fluorescence and polarization measurements. The volume concentration, V_i, of i-th aerosol

288 component can be estimated from the backscattering coefficient using the corresponding lidar ratio,

289 S_{532}^i, and the extinction-to-volume conversion factors C_V^i (Mamouri and Ansmann, 2017;

290 Ansmann et al., 2019, 2021; He et al., 2023). Thus, for the i-th aerosol component:

291 $$V_i = \beta_{532} \times \eta_i \times S_{532}^i \times C_V^i \tag{8}$$

292 The values of the conversion factors at 532 nm, derived from AERONET observations, along with

293 some reported lidar ratios, are summarized in Table 2. Therefore, the presented information allows

294 us to quantify the composition of the aerosol mixture.

295

296 Table 2. Lidar ratios (S_{532}^i) and extinction-to-volume conversion factors (C_V^i) for different types

297 of aerosol.

Type	Lidar ratio S_{532}^i , sr	C_V^i , µm³cm⁻³/Mm⁻¹
Urban	53-70 [1]	0.3-0.41 [2]
Smoke (North American, aged)	55-73 [1] 50-78[5]	0.13 [4]
Dust (North Africa)	40-50 [4]	0.61-0.64 [2] 0.67-0.73 [3] 0.64-0.67 [6]

298 [1]Burton et al., 2013; [2]Mamouri and Ansmann, 2017; [3]Ansmann et al., 2019; [4]Ansmann et al., 2021; [5]Hu et al.,
299 2022; [6]He et al., 2023.
300

3.4. Heatwave over Lille in July 2022.

302   The heatwave in France in July 2022 was attributed to a high-pressure system known as the

303 Azores High, which usually sits off Spain and pushed farther north, resulting in elevated

304 temperatures and multiple fires. The Sun photometer and lidar observations at ATOLL consistently

305 recorded an increase in aerosol content over Lille in the middle of July 2022. Fig.11 displays the

306 aerosol optical depth (AOD) at 500 nm and the Angstrom exponent for 380/500 nm wavelengths

307 provided by AERONET. Lidar observations were performed from July 16 to July 23, as shown in

308 the frame in Fig.10. Within this interval, the optical depth increased, reaching its peak on July 18.

309 The Angstrom exponent decreased, indicating the presence of dust. Fig.11 shows the column-

310 integrated particle volume, provided by AERONET, presented separately for the fine and coarse

311 mode particles. After July 16, the volume of the coarse mode increased approximately fourfold,

312 while the fine mode did not show significant changes, further supporting the presence of dust

313 particles. Unfortunately, volume retrievals are not available after July 20 due to the presence of

314 clouds. The methodology outlined in Sect. 2.2 was used to analyze the composition of aerosols

315 during the heatwave.

316   In Fig.13, we can see the spatiotemporal distributions of β_{532}, δ_{532} and G_F for four

317 measurement sessions between July 16 and July 23, 2022. On July 16-17, after midnight, a dust

318 layer with δ_{532} exceeding 20% appeared at a height of 5 km. The following night (July 17-18), the

319 lower border of the dust layer descended to 2 km. By the night of July 18-19, we observed strong

aerosol backscattering (above 1.0 Mm^{-1}sr^{-1}) from the ground up to a height of 5 km. Dust was primarily found within two height ranges: 0.75-2.0 km and 3.0-5.0 km, where the particle depolarization ratio δ_{532} exceeded 20%. The aerosol between these dust layers showed high fluorescence capacity (above 2.0×10^{-4}), indicating the presence of smoke. Unfortunately, we could not make long-term lidar observations from July 19-21 due to cloud cover. However, by the night of July 22-23, we observed localized aerosols below 3 km. The values of δ_{532} and G_F were below 10% and 1.0×10^{-4}, respectively, which is typical for urban particles. The relative humidity during the measurements for July 16-19 was below 60 % within the height range being considered. On the night of July 22-23, the relative humidity was higher, reaching up to 80%. In Fig.14, we provide the G_F-δ_{532} diagrams for the measurements shown in Fig.13. On the night of July 16-17, the clusters corresponding to dust and smoke/urban particles are distinct. However, for July 17-19, dust was mixed with smoke and urban particles, resulting in a characteristic pattern on the G_F-δ_{532} diagram (Veselovskii et al., 2022). By the night of July 22-23, only one cluster, corresponding to urban aerosol, was observed. The distributions of particle types in Fig.14 for the period of July 16-19 contain extended gray regions where different types of particles are mixed and cannot be identified. In Fig.15, we can see the partition technique used to evaluate the contributions of dust, smoke, and urban aerosol to β_{532}. From this analysis, we can conclude that on the night of July 16-17, the aerosol below 2.5 km was a mixture of smoke and urban particles, and the elevated dust layer (00:00-03:00 UTC) contained a significant amount of urban particles (η_u is up to 0.4). On July 18-19, the aerosol between the two dust layers, within the height range of 2-3 km, was also a mixture of smoke and urban particles.

The aerosol classification based on fluorescence and depolarization measurements is supported by the analysis of backward trajectories. Fig.16 shows the five-day backward trajectories for four measurement sessions from Figure 15 at altitudes of 1500 m, 3000 m, and 4500 m. On July 16-17, the dust layer above 4000 m originates from North Africa, while smoke at 3000 m is likely transported from North America. The air masses at 3000 m on July 17-18 are transported from Africa over regions of wildfires in Spain, indicating a mixture of dust and smoke. Smoke at 3000 m on July 18-19 again originates from wildfires in Spain, while the source of the dust layers at 1500 m and 4000 m is in Africa. Finally, on July 22-23, the heat wave was over. The air masses arrive from the West outside dust and smoke sources, and aerosol in Fig. 15 within the 1000-3000 m range is identified as urban.

351   As mentioned, the volume concentration of each component can be estimated using Eq. 8.

352 Fig.17 presents the vertical profiles of volume concentration for smoke, urban, and dust particles

353 for four measurement sessions from Fig.15. In the calculations, we used the mean values of η_s, η_u,

354 η_d, as well as the mean values of the lidar ratios and fluorescence capacity from Table 2. The lidar

355 ratios used for smoke, urban, and dust are 64 sr, 61 sr, and 45 sr, respectively, and the fluorescence

356 capacity values are 0.13×10^{-4}, 0.35×10^{-4}, and 0.7×10^{-4}. The main contributors to the volume are

357 urban and dust particles, with smoke contributing noticeably only on July 18 and 19, but with a

358 volume density still below 5 $\mu m^3 cm^{-3}$. The volume concentration can be recalculated to the mass

359 concentration, if the particle density is known. The profiles of mass concentration are shown in

360 Fig.17 as dash lines. In computations we utilized a smoke density of ρ_s=1.15 g/cm^3 (Ansmann et

361 al., 2021) and a dust density of ρ_d=2.6 g/cm^3 (He et al., 2023). For urban aerosol a density of

362 ρ_u=1.5 g/cm^3 was selected for sulfate particles.

363   To assess the validity of our volume estimations, we compared our results with AERONET

364 retrievals. For this comparison, the volume density profiles of each component from Fig.17 were

365 extrapolated to the ground, and the total column-integrated volume was calculated. The results are

366 depicted in Fig.12 by stars, with an additional measurement on July 19 (22:00-23:00) included. It

367 is evident that the results provided by AERONET are in reasonable agreement with the results

368 provided by the lidar.

369

370 **Conclusion**

371   In conclusion, this study introduces an approach to partition aerosol mixtures in terms of

372 backscattering coefficients, based on fluorescence and polarization lidar measurements.

373 Specifically, we used the particle depolarization ratio at 532 nm and the fluorescence capacity,

374 allowing for the partitioning of a three-component aerosol mixture at every height/time pixel. The

375 robustness of this approach is demonstrated through testing with Mie-Raman-fluorescence lidar

376 observations at the ATOLL instrumental site, providing valuable insights into the composition and

377 dynamics of atmospheric aerosols. One notable advantage of the proposed approach is its

378 applicability even in conditions of low aerosol content or for aerosol layers in the upper

379 troposphere, where deriving profiles of extinction coefficients might be challenging. Additionally,

380 backscattering coefficients of aerosol components can be converted to particle volume densities

381 using corresponding lidar ratios along with extinction-to-volume conversion factors. While this

382 conversion provides a rough volume estimation, considering the variability of the lidar ratios and

383 the conversion factors within a given aerosol type, a comparison of lidar-derived particle volume

384 during the heatwave over Lille in July 2022 demonstrates promising agreement with AERONET

385 retrievals. At this stage, we have simplified our classification scheme by incorporating four aerosol

386 types: smoke, dust, pollen, and urban particles. It is important to note that the use of fluorescence

387 is an efficient way to distinguish between urban and smoke particles, which is a challenge for other

388 methods that do not utilize fluorescence. However, we recognize the need to expand our approach

389 to include additional aerosol types, particularly those with strong absorption such as polluted urban

390 aerosol. This expansion will involve incorporating additional particle parameters, like lidar ratios,

391 and is planned for our future research. It is crucial to acknowledge that the particle hygroscopic

392 growth complicates the use of fluorescence capacity, resulting in increased uncertainty. To address

393 this, we aim to utilize the additional independent information about aerosol type provided by the

394 fluorescence spectrum. Importantly, the fluorescence spectrum is not affected by relative humidity.

395 In our future research, we plan to further enhance the fluorescence capabilities by increasing the

396 number of fluorescence channels in the lidar.

397

398 *Data availability*. Lidar measurements are available upon request
399 (philippe.goloub@univ-lille.fr).
400
401 *Author contributions*. IV processed the data and wrote the paper. BB prepared the program for
402 aerosol mixture partitioning. QH performed meteorological analysis. TP, GD and WB performed
403 lidar measurements in Lille. PG supervised the project and helped with paper preparation. MK and
404 NK participated in algorithms development and data analysis.
405 .
406 *Competing interests*. The authors declare that they have no conflict of interests.

407

408 **Acknowledgement**

409 We acknowledge funding from the CaPPA project funded by the ANR through the PIA under

410 contract ANR-11-LABX-0005-01, the "Hauts de France" Regional Council (project ECRIN) and

411 the European Regional Development Fund (FEDER). ESA/QA4EO program is greatly

412 acknowledged for supporting the observation activity at LOA. The work of Q. Hu was supported

413 by Agence *Nationale* de Recherhce ANR (*ANR-21-ESRE-0013) through the* OBS4CLIM project

414 and development of algorithm was performed in the frame of project 21-17-00114 of Russian

Science Foundation. This work has also benefited from the support of the research infrastructure ACTRIS-FR, registered on the Roadmap of the French Ministry of Research

References

Ansmann, A., Mamouri, R.-E., Hofer, J., Baars, H., Althausen, D., and Abdullaev, S. F.: Dust mass, cloud condensation nuclei, and ice-nucleating particle profiling with polarization lidar: updated POLIPHON conversion factors from global AERONET analysis, Atmos. Meas. Tech., 12, 4849–4865, https://doi.org/10.5194/amt-12-4849-2019, 2019.

Ansmann, A., Ohneiser, K., Mamouri, R.-E., Knopf, D. A., Veselovskii, I., Baars, H., Engelmann, R., Foth, A., Jimenez, C., Seifert, P., and Barja, B.: Tropospheric and stratospheric wildfire smoke profiling with lidar: Mass, surface area, CCN and INP retrieval, Atmos. Chem. Phys., 21, 9779–9807, https://doi.org/10.5194/acp-21-9779-2021, 2021.

Burton, S. P., Ferrare, R. A., Hostetler, C. A., Hair, J.W., Rogers, R. R., Obland, M. D., Butler, C. F., Cook, A. L., Harper, D. B., and Froyd, K. D.: Aerosol classification using airborne High Spectral Resolution Lidar measurements – methodology and examples, Atmos. Meas. Tech., 5, 73–98, https://doi.org/10.5194/amt-5-73-2012, 2012.

Burton, S. P., Ferrare, R. A., Vaughan, M. A., Omar, A. H., Rogers, R. R., Hostetler, C. A., and Hair, J. W.: Aerosol classification from airborne HSRL and comparisons with the CALIPSO vertical feature mask, Atmos. Meas. Tech., 6, 1397–1412, https://doi.org/10.5194/amt-6-1397-2013, 2013.

Burton, S. P., Vaughan, M. A., Ferrare, R. A., and Hostetler, C. A.: Separating mixtures of aerosol types in airborne High Spectral Resolution Lidar data, Atmos. Meas. Tech., 7, 419–436, https://doi.org/10.5194/amt-7-419-2014, 2014.

Cao, X., Roy, G., and Bernier, R.: Lidar polarization discrimination of bioaerosols, Opt. Eng., 49, 116201, https://doi.org/10.1117/1.3505877, 2010.

Cholleton, D.; Rairoux, P.; Miffre, A.: Laboratory evaluation of the (355, 532) nm particle depolarization ratio of pure pollen at 180.0 lidar backscattering angle. Remote Sens. 14, 3767, https://doi.org/10.3390/rs14153767, 2022.

Dubovik, O., Holben, B. N., Eck, T. F., Smirnov, A., Kaufman, Y. J., King, M. D., Tanre, D., and Slutsker, I.: Variability of absorption and optical properties of key aerosol types observed in

worldwide locations, J. Atmos. Sci., 59, 590–608, 2002. https://doi.org/10.1175/1520-0469(2002)059<0590:voaaop>2.0.co;2

Floutsi, A. A., Baars, H., Engelmann, R., Althausen, D., Ansmann, A., Bohlmann, S., Heese, B., Hofer, J., Kanitz, T., Haarig, M., Ohneiser, K., Radenz, M., Seifert, P., Skupin, A., Yin, Z., Abdullaev, S. F., Komppula, M., Filioglou, M., Giannakaki, E., Stachlewska, I. S., Janicka, L., Bortoli, D., Marinou, E., Amiridis, V., Gialitaki, A., Mamouri, R.-E., Barja, B., and Wandinger, U.: DeLiAn – a growing collection of depolarization ratio, lidar ratio and Ångström exponent for different aerosol types and mixtures from ground-based lidar observations, Atmos. Meas. Tech., 16, 2353–2379, https://doi.org/10.5194/amt-16-2353-2023, 2023a.

Floutsi, A. A., Baars, H., and Wandinger, U.: HETEAC-Flex: An optimal estimation method for aerosol typing based on lidar-derived intensive optical properties, EGUsphere [preprint], https://doi.org/10.5194/egusphere-2023-1880, 2023b.

Freudenthaler,V., Esselborn, M.,Wiegner, M.,Heese, B., Tesche, M. and co-authors: Depolarization ratio profiling at several wavelengths in pure Saharan dust during SAMUM 2006, *Tellus* 61B, 165–179, doi:10.1111/j.1600-0889.2008.00396.x, 2009.

Groß, S., Esselborn, M., Weinzierl, B., Wirth, M., Fix, A., and Petzold, A.: Aerosol classification by airborne high spectral resolution lidar observations, Atmos. Chem. Phys., 13, 2487–2505, https://doi.org/10.5194/acp-13-2487-2013, 2013.

Hara, Y., Nishizawa, T., Sugimoto , N., Osada, K., Yumimoto, K., Uno, I., Kudo, R., and Ishimoto, H.: Retrieval of aerosol components using multi-wavelength Mie-Raman lidar and comparison with ground aerosol sampling, Remote Sens., 10, 937, 2018. https://doi:10.3390/rs10060937

He, Y., Yin, Z., Ansmann, A., Liu, F., Wang, L., Jing, D., and Shen, H.: POLIPHON conversion factors for retrieving dust-related cloud condensation nuclei and ice-nucleating particle concentration profiles at oceanic sites, Atmos. Meas. Tech., 16, 1951–1970, https://doi.org/10.5194/amt-16-1951-2023, 2023.

Hu, Q., Goloub, P., Veselovskii, I., and Podvin, T.: The characterization of long-range transported North American biomass burning plumes: what can a multi-wavelength Mie–Raman-polarization-fluorescence lidar provide?, Atmos. Chem. Phys., 22, 5399–5414, https://doi.org/10.5194/acp-22-5399-2022, 2022.

Mamouri, R.-E., and Ansmann, A.: Potential of polarization/Raman lidar to separate fine dust, coarse dust, maritime, and anthropogenic aerosol profiles, Atmos. Meas. Tech., 10, 3403–3427, https://doi.org/10.5194/amt-10-3403-2017, 2017.

Miffre, A., Cholleton, D., and Rairoux, P.: On the use of light polarization to investigate the size, shape, and refractive index dependence of backscattering Ångström exponents, Opt. Lett. 45, 1084-1087, https://doi.org/10.1364/OL.385107, 2020.

Mylonaki, M., Giannakaki, E., Papayannis, A., Papanikolaou, C.-A., Komppula, M., Nicolae, D., Papagiannopoulos, N., Amodeo, A., Baars, H., and Soupiona, O.: Aerosol type classification analysis using EARLINET multiwavelength and depolarization lidar observations, Atmos. Chem. Phys., 21, 2211–2227, https://doi.org/10.5194/acp-21-2211-2021, 2021.

Nicolae, D., Vasilescu, J., Talianu, C., Binietoglou, I., Nicolae, V., Andrei, S., and Antonescu, B.: A neural network aerosol-typing algorithm based on lidar data, Atmos. Chem. Phys., 18, 14511–14537, https://doi.org/10.5194/acp-18-14511-2018, 2018.

Ohneiser, K., Ansmann, A., Baars, H., Seifert, P., Barja, B., Jimenez, C., Radenz, M., Teisseire, A., Floutsi, A., Haarig, M., Foth, A., Chudnovsky, A., Engelmann, R., Zamorano, F., Bühl, J., and Wandinger, U.: Smoke of extreme Australian bushfires observed in the stratosphere over Punta Arenas, Chile, in January 2020: optical thickness, lidar ratios, and depolarization ratios at 355 and 532 nm, Atmos. Chem. Phys., 20, 8003–8015, https://doi.org/10.5194/acp-20-8003-2020, 2020.

Papagiannopoulos, N., Mona, L., Amodeo, A., D'Amico, G., Gumà Claramunt, P., Pappalardo, G., Alados-Arboledas, L., Guerrero- Rascado, J. L., Amiridis, V., Kokkalis, P., Apituley, A., Baars, H., Schwarz, A.,Wandinger, U., Binietoglou, I., Nicolae, D., Bortoli, D., Comerón, A., Rodríguez-Gómez, A., Sicard, M., Papayannis, A., and Wiegner, M.: An automatic observation-based aerosol typing method for EARLINET, Atmos. Chem. Phys., 18, 15879– 15901, https://doi.org/10.5194/acp-18-15879-2018, 2018.

Reichardt, J., Leinweber, R., Schwebe, A.: Fluorescing aerosols and clouds: investigations of co-existence, EPJ Web Conf., 176, 05010, https://doi.org/10.1051/epjconf/201817605010, 2018.

Reichardt, J., Behrendt, O., and Lauermann, F.: Spectrometric fluorescence and Raman lidar: absolute calibration of aerosol fluorescence spectra and fluorescence correction of humidity measurements, Atmos. Meas. Tech., 16, 1–13, https://doi.org/10.5194/amt-16-1-2023, 2023.

505 Stein, A. F., Draxler, R. R., Rolph, G. D., Stunder, B. J. B., Cohen, M. D., and Ngan, F.: NOAA's
506   HYSPLIT atmospheric transport and dispersion modeling system, B. Am. Meteorol. Soc., 96,
507   2059–2077, https://doi.org/10.1175/BAMS-D-14-00110.1, 2015.

508 Sugimoto, N. and Lee, C. H.: Characteristics of dust aerosols inferred from lidar depolarization
509   measurements at two wavelengths, Appl. Optics, 45, 7468–7474,
510   https://doi.org/10.1364/AO.45.007468, 2006.

511 Tesche, M., Ansmann, A., Müller, D., Althausen, D., Engelmann, R., Freudenthaler, V., and Groß,
512   S.: Vertically resolved separation of dust and smoke over Cape Verde using multiwavelength
513   Raman and polarization lidars during Saharan Mineral Dust Experiment 2008, J. Geophys. Res.,
514   114, D13202, doi:10.1029/2009JD011862, 2009.

515 Veselovskii, I., Hu, Q., Goloub, P., Podvin, T., Korenskiy, M., Pujol, O., Dubovik, O., Lopatin,
516   A.: Combined use of Mie-Raman and fluorescence lidar observations for improving aerosol
517   characterization: feasibility experiment, Atm. Meas. Tech., 13, 6691–6701,
518   doi.org/10.5194/amt-13-6691-2020, 2020.

519 Veselovskii, I., Hu, Q., Goloub, P., Podvin, T., Choël, M., Visez, N., and Korenskiy, M.: Mie–
520   Raman–fluorescence lidar observations of aerosols during pollen season in the north of France,
521   Atm. Meas. Tech., 14, 4773–4786, doi.org/10.5194/amt-14-4773-2021, 2021.

522 Veselovskii, I., Hu, Q., Goloub, P., Podvin, T., Barchunov, B., and Korenskii, M.: Combining
523   Mie–Raman and fluorescence observations: a step forward in aerosol classification with lidar
524   technology, Atmos. Meas. Tech., 15, 4881–4900, https://doi.org/10.5194/amt-15-4881-2022,
525   2022.

526 Veselovskii, I., Hu, Q., Goloub, P., Podvin, T., Boissiere, W., Korenskiy, M., Kasianik, N.,
527   Khaykin, S., and Miri, R.: Derivation of aerosol fluorescence and water vapor Raman
528   depolarization ratios from lidar measurements, Atmos. Meas. Tech., 17, 1023–1036,
529   https://doi.org/10.5194/amt-17-1023-2024, 2024.

530 Voudouri, K. A., Siomos, N., Michailidis, K., Papagiannopoulos, N., Mona, L., Cornacchia, C.,
531   Nicolae, D., and Balis, D.: Comparison of two automated aerosol typing methods and their
532   application to an EARLINET station, Atmos. Chem. Phys., 19, 10961–10980,
533   https://doi.org/10.5194/acp-19-10961-2019, 2019.

534 Zhang, Y., Sun, Z., Chen, S., Chen, H., Guo, P., Chen, S., He, J., Wang, J., Nian, X.: Classification
535   and source analysis of low-altitude aerosols in Beijing using fluorescence–Mie polarization

536   lidar, Optics Communications, 479, 126417, https://doi.org/10.1016/j.optcom.2020.126417,

537   2021.

538 Wandinger, U., Floutsi, A. A., Baars, H., Haarig, M., Ansmann, A., Hünerbein, A., Docter, N.,

539   Donovan, D., van Zadelhoff, G.-J., Mason, S., and Cole, J.: HETEAC – the Hybrid End-To-

540   End Aerosol Classification model for EarthCARE, Atmos. Meas. Tech., 16, 2485–2510,

541   https://doi.org/10.5194/amt-16-2485-2023, 2023.

542 Wang, N., Shen, X., Xiao, D., Veselovskii, I., Zhao,C., Chen, F., Liu, C., Rong, Y., Ke, J., Wang,

543   B., Qi, B., Liu, D.: Development of ZJU high-spectral-resolution lidar for aerosol and cloud:

544   feature detection and classification, Journal of Quantitative Spectroscopy & Radiative Transfer,

545   v.261, 107513, doi.org/10.1016/j.jqsrt.2021.107513, 2021.

546

547
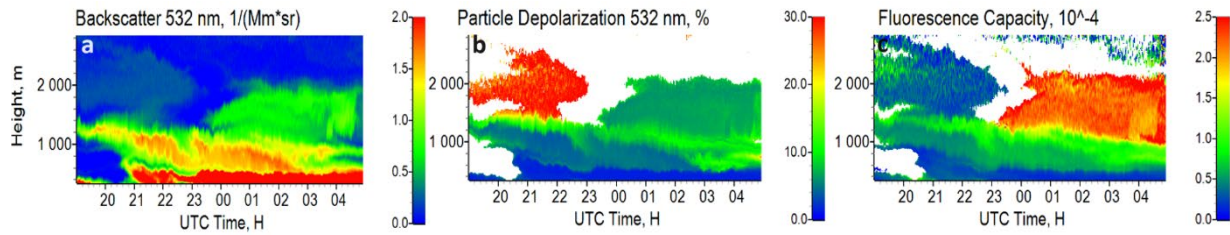
548

549 Fig.1. Spatiotemporal distributions of (a) the backscattering coefficient at 532 nm, (b) particle

550 depolarization ratio at 532 nm and (c) fluorescence capacity during the night of March 27-28,

551 2022. The depolarization ratio and fluorescence capacity are calculated only for the values $\beta_{532}>0.1$

552 $Mm^{-1}sr^{-1}$. The measurements were taken at an angle of 45^0 to the horizon.

553

554

555

556

557
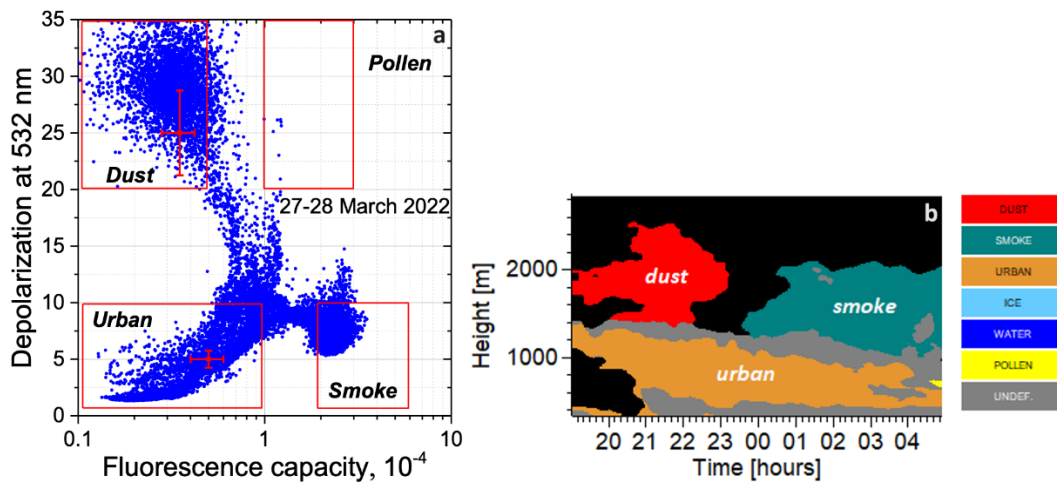
558 Fig.2. (a) The δ_{532}-G_F diagram for observations in the height range of 350 m–2800 m and (b) the

559 spatiotemporal distribution of aerosol types during the night of March 27–28, 2022.

560
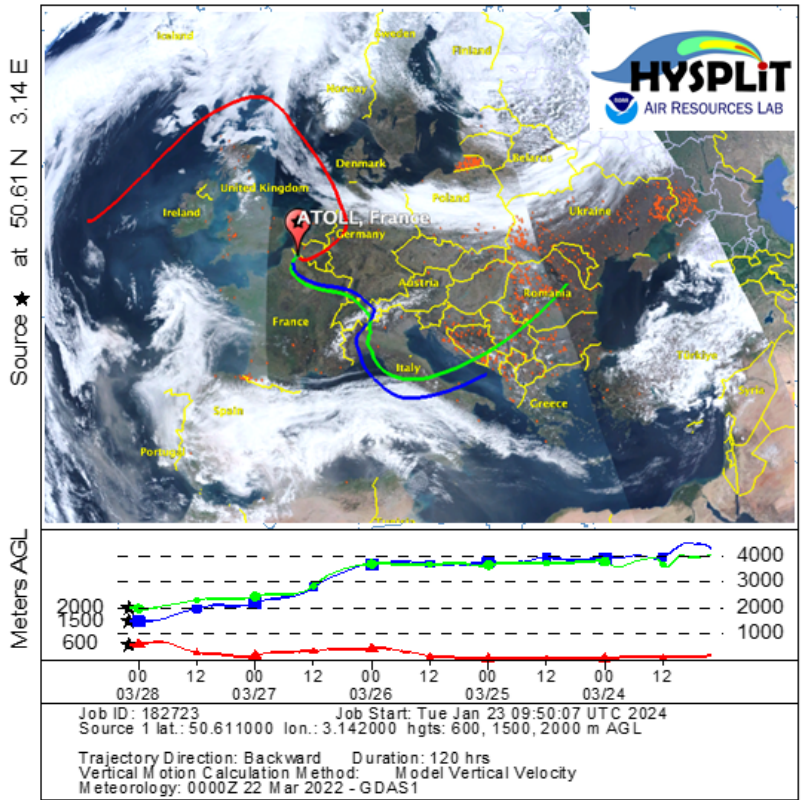
561

562 Fig.3. The HYSPLIT five-day backward trajectories for the air mass over Lille at altitudes 600 m,

563 1500 m, and 2000 m on March 28, 2022 at 02:00 UTC. Red dots depict the regions of forest fires.

564

565

566
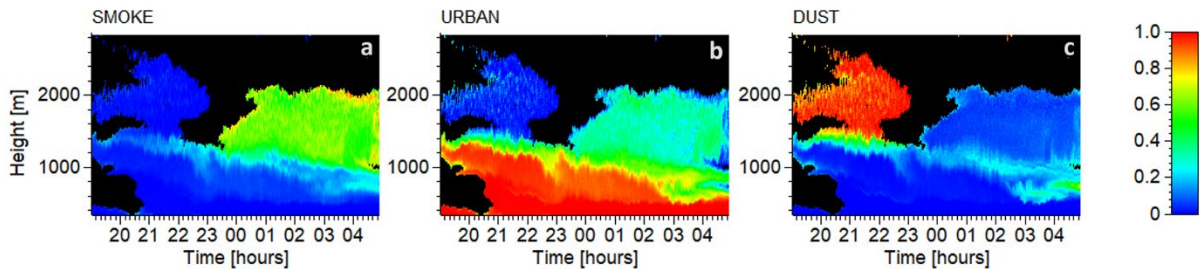
567

568 Fig.4. Relative contributions of (a) smoke (η_s), (b) urban (η_u), and (c) dust (η_d) particles to the

569 backscattering coefficient β_{532} during the night of March 27–28, 2022.

570
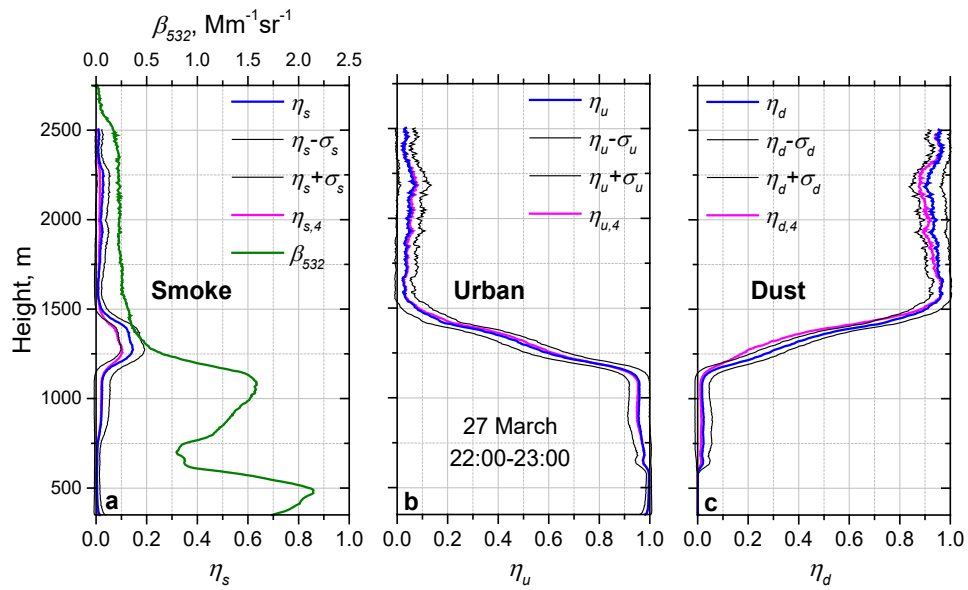
573   Fig.5. Vertical profiles of the relative contributions of smoke (η_s), urban (η_u), and dust (η_d) particles

574   to the backscattering coefficient β_{532} on March 27, 2022. These profiles are derived under the

575   assumption that only three aerosol types occur. The black lines depict the deviation of solutions

576   from the mean value ($\eta_i \pm \sigma_i$). Magenta lines show the relative contributions of smoke, urban and

577   dust particles ($\eta_{s,4}$, $\eta_{u,4}$, $\eta_{d,4}$) when four aerosol types (including pollen) are considered.

578

579

580
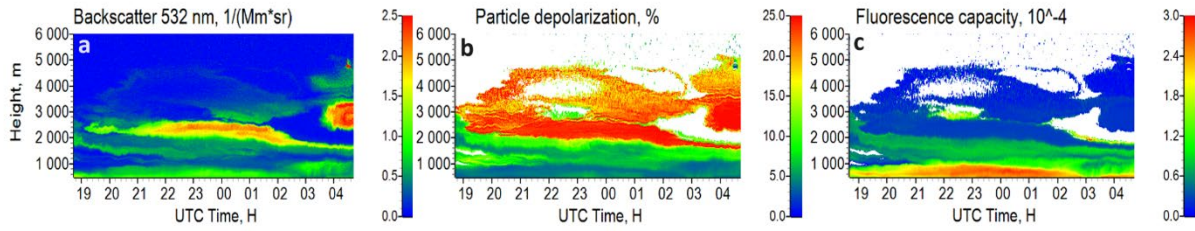
Fig.6. Spatiotemporal distributions of (a) the backscattering coefficient at 532 nm, (b) particle depolarization ratio at 532 nm and (c) fluorescence capacity during the night of October 1-2, 2023. The depolarization ratio and fluorescence capacity are calculated only for values of $\beta_{532}>0.1$ Mm^{-1}sr^{-1}.

585

586
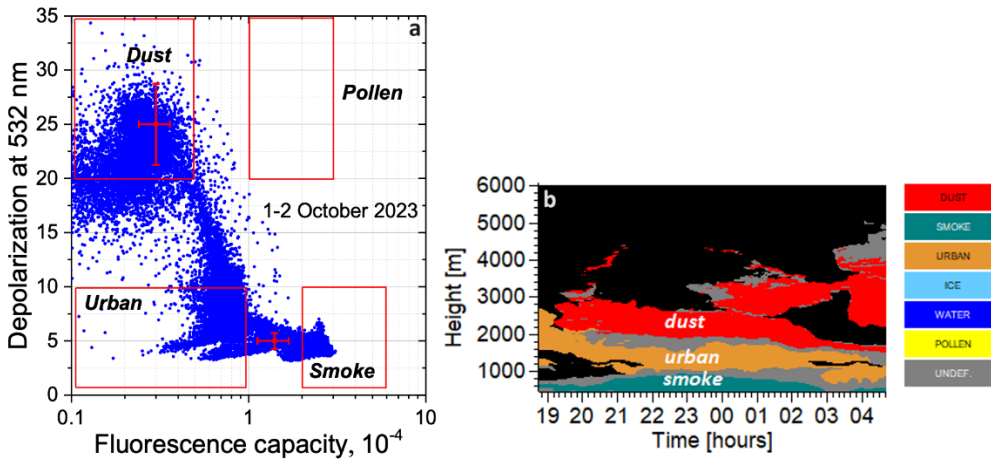
Fig.7. (a) The δ_{532}-G_F diagram and (b) the spatiotemporal distribution of aerosol types during the night of October 1-2, 2023.

589
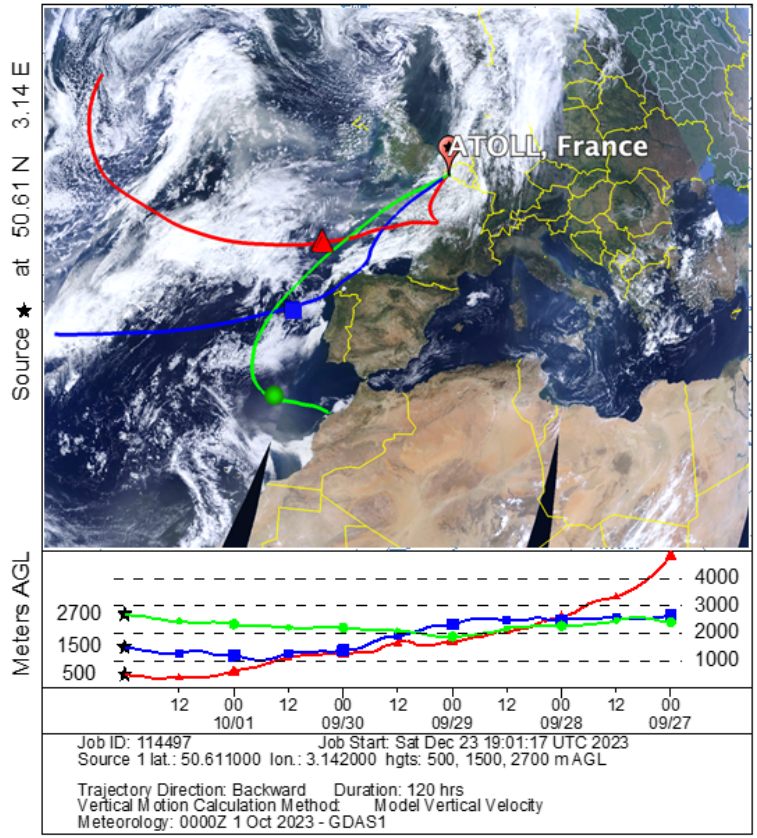
590

591 Fig.8. The HYSPLIT five-day backward trajectories for the air mass over Lille at altitudes 500 m,

592 1500 m, and 2700 m on October 2, 2023 at 00:00 UTC.

593

594
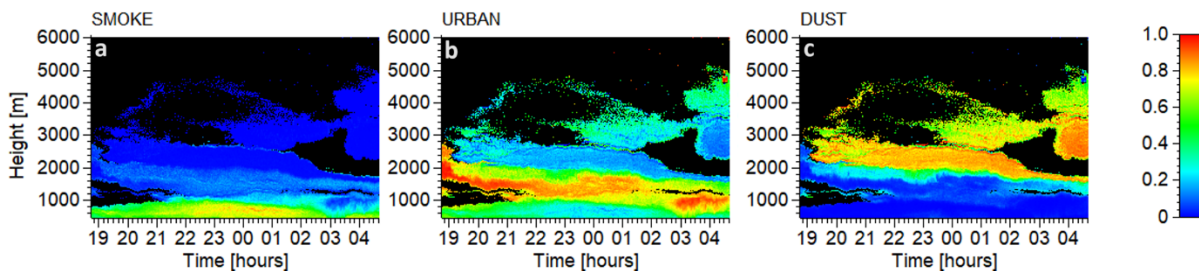
595

596   Fig.9. The relative contributions of (a) smoke (η_s), (b) urban (η_u), and (c)dust (η_d) particles to the

597   backscattering coefficient β_{532} during the night of October 1-2, 2023.

598

599

600

601
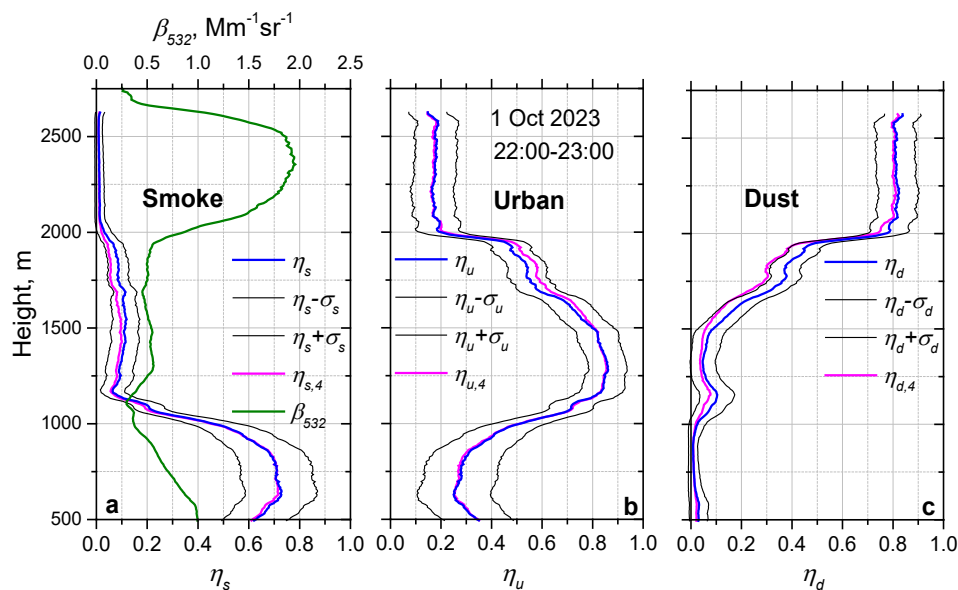
602

603   Fig.10. Vertical profiles of the relative contributions of smoke (η_s), urban (η_u), and dust (η_d)

604   particles to the backscattering coefficient β_{532} on October 1, 2023. The profiles are derived under

605   the assumption that only three aerosol types occur. The black lines depict the deviation of solutions

606   from the mean value ($\eta_i \pm \sigma_i$). The magenta lines show the relative contributions of smoke, dust and

607   urban particles ($\eta_{s,4}$, $\eta_{u,4}$, $\eta_{d,4}$) when four aerosol types (including pollen) are considered.

608

609
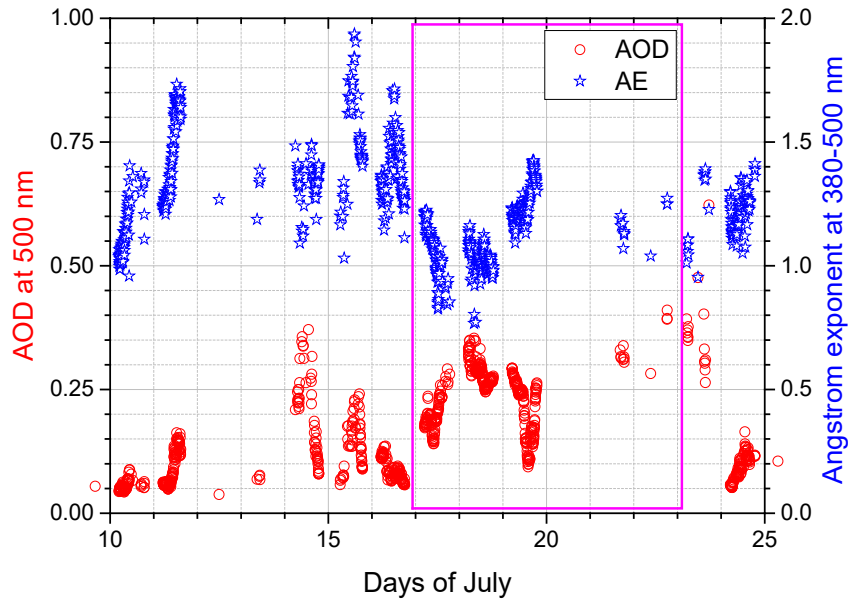
610

611 Fig.11. The aerosol optical depth (AOD) at 500 nm and the Angstrom exponent (AE) provided by

612 AERONET over Lille in July 2022. Magenta box depicts the time period during which lidar

613 observations in this study were analyzed.
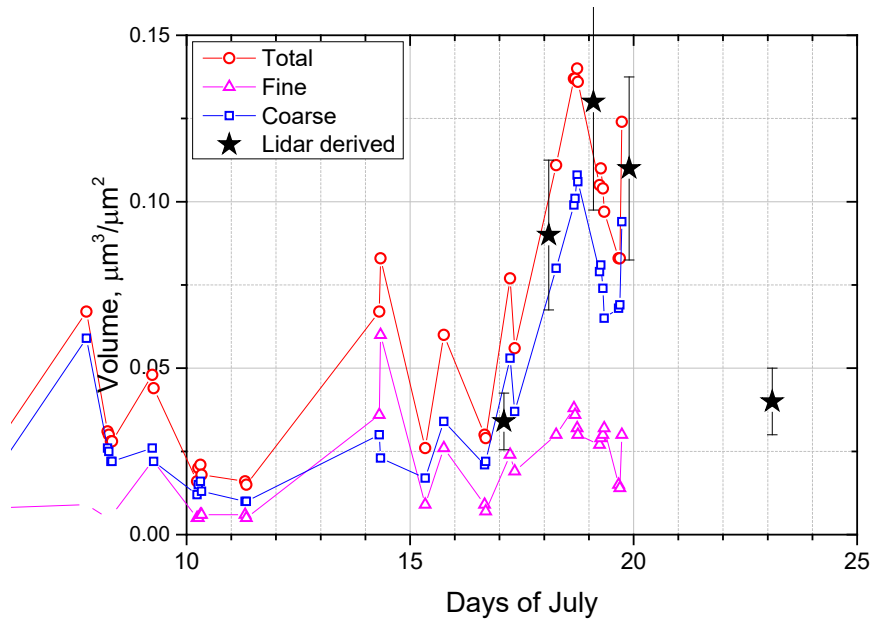
614

615 Fig.12. Column-integrated aerosol volume (circles) in July 2022 provided by AERONET. The

616 triangles and squares represent the volumes of the fine and coarse modes, respectively. Black stars

617 depict the total particle volume derived from lidar observations.

618

619

620

621

622
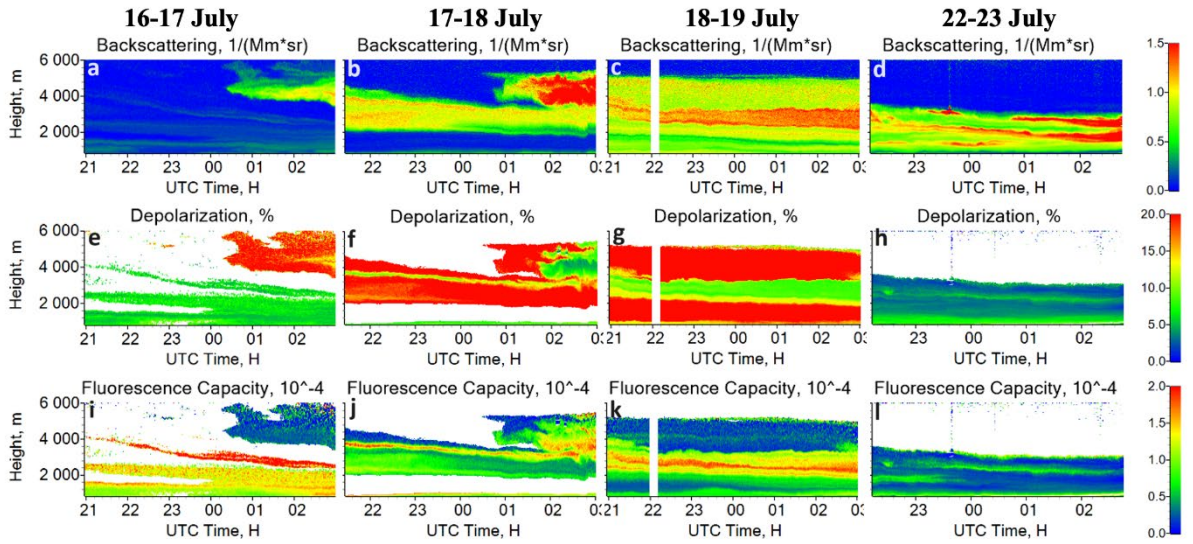
Fig.13. Spatiotemporal distributions of (a-d) the backscattering coefficient β_{532}, (e-h) the particle depolarization ratio δ_{532}, and (i-l) the fluorescence capacity G_F for the nights of July 16-17, 17-18, 18-19 and 22-23, 2022. The depolarization ratio and fluorescence capacity are calculated only for the values $\beta_{532} > 0.1$ $Mm^{-1}sr^{-1}$.

627

628
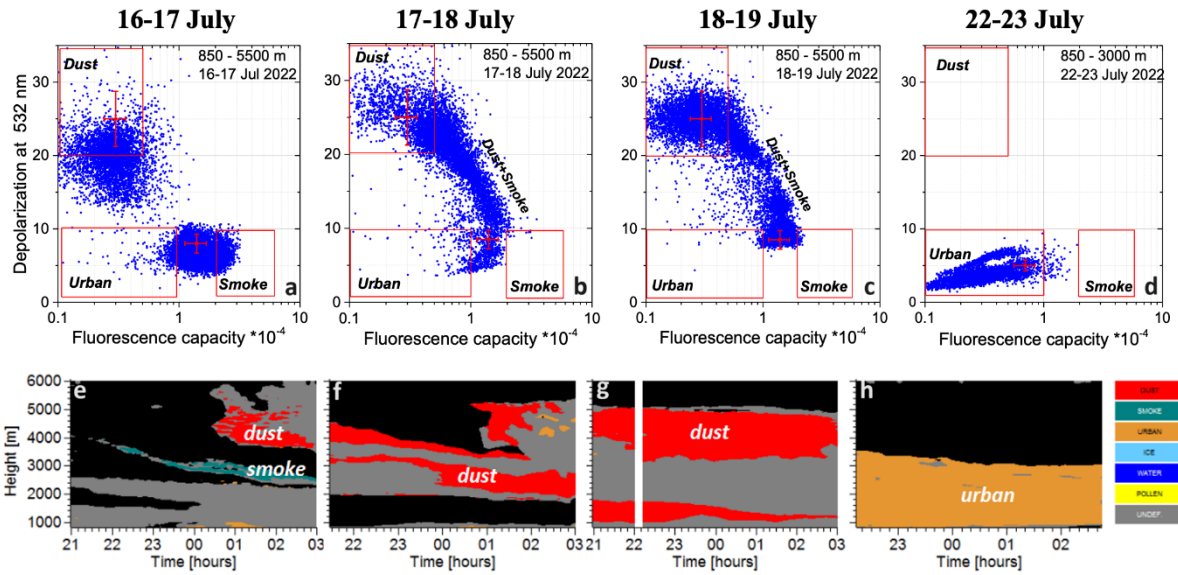
629

630

631   Fig.14. (a-d) The δ_{532}-G_F diagram and (e-h) the spatiotemporal distribution of aerosol types for the

632   nights of July 16-17, 17-18, 18-19 and 22-23, 2022. The grey coloring represents an undefined

633   aerosol type.

634

635

636
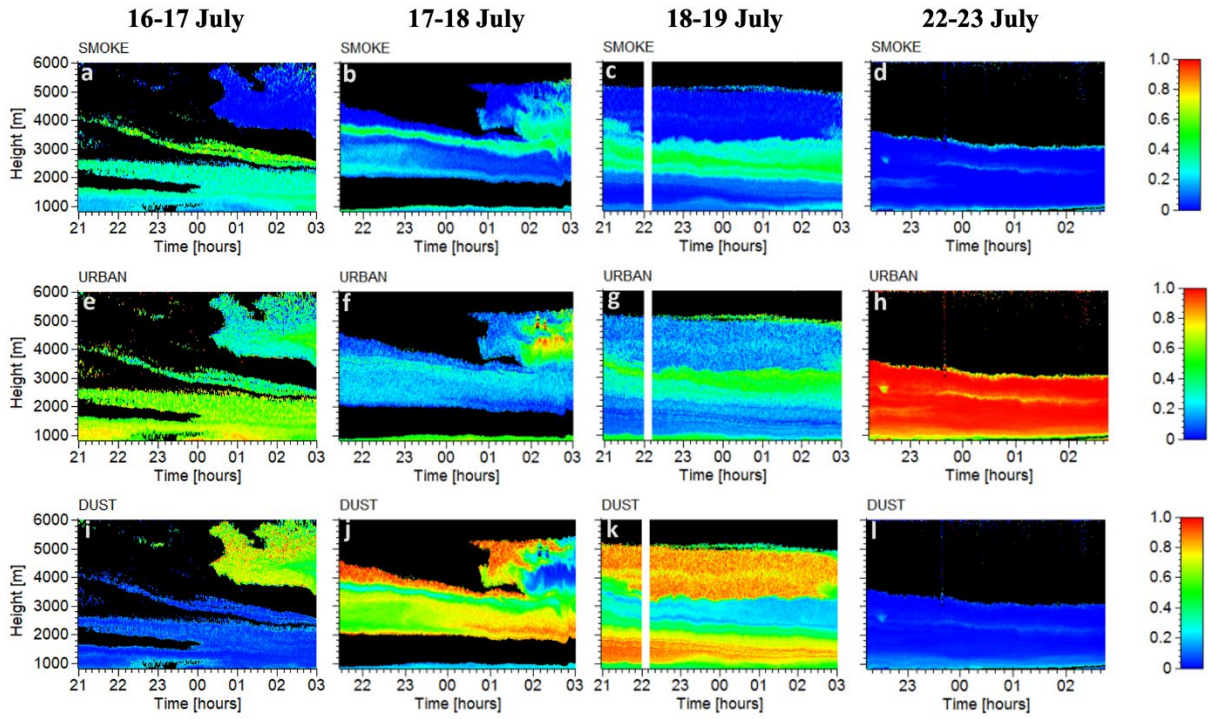
637

638 Fig.15. The relative contributions of (a-d) smoke, (e-h) urban and (i-l) dust particles to the
639 backscattering coefficient at 532 nm for the nights of July 16-17, 17-18, 18-19 and 22-23, 2022.
640

641

642

643

644
645
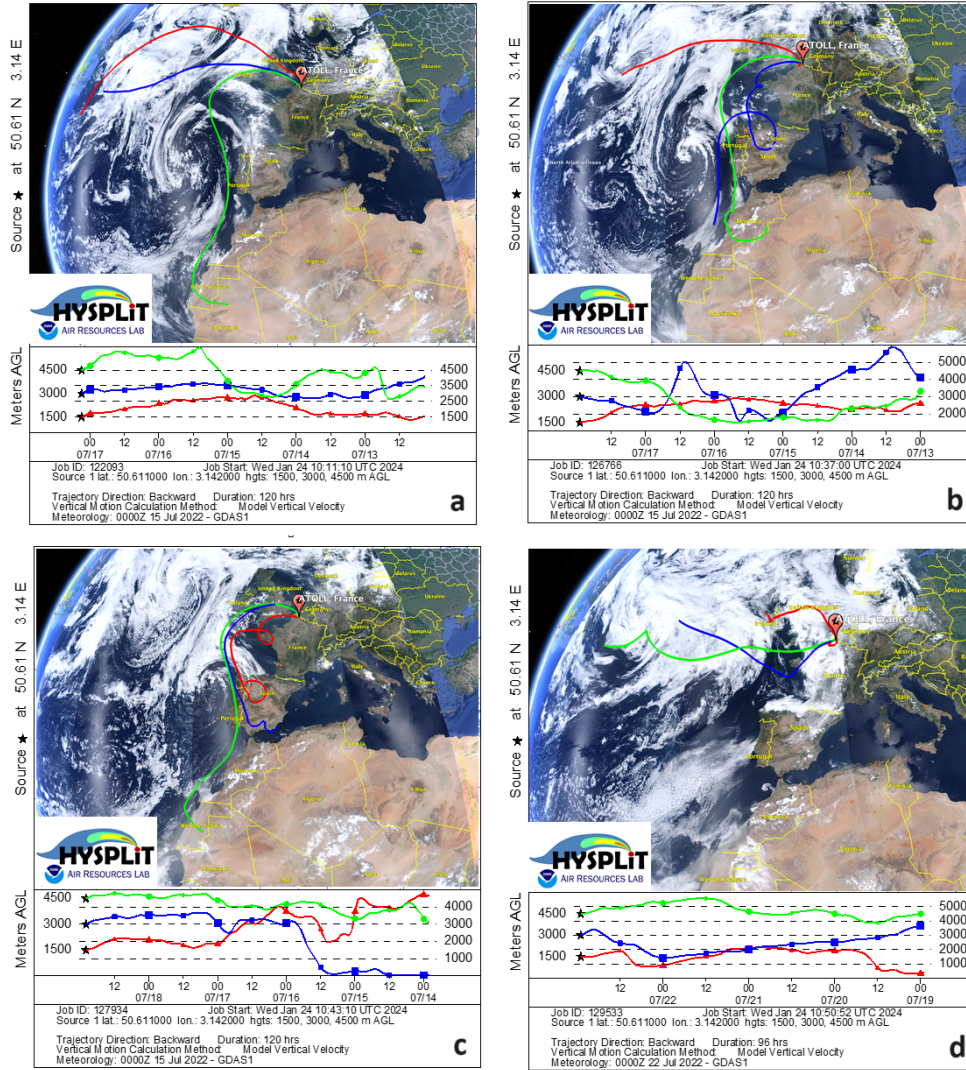
646   Fig.16. The HYSPLIT five-day backward trajectories for the air mass over Lille at altitudes 1500

647   m, 3000 m, and 4500 m on (a) July 17, 2022 at 03:00 UTC; (b) July 17, 2022 at 23:00 UTC; (c)

648   July 18, 2022 at 22:00 UTC; (d) July 22, 2022 at 22:00 UTC. Red dots depict the regions of forest

649   fires.

650

651
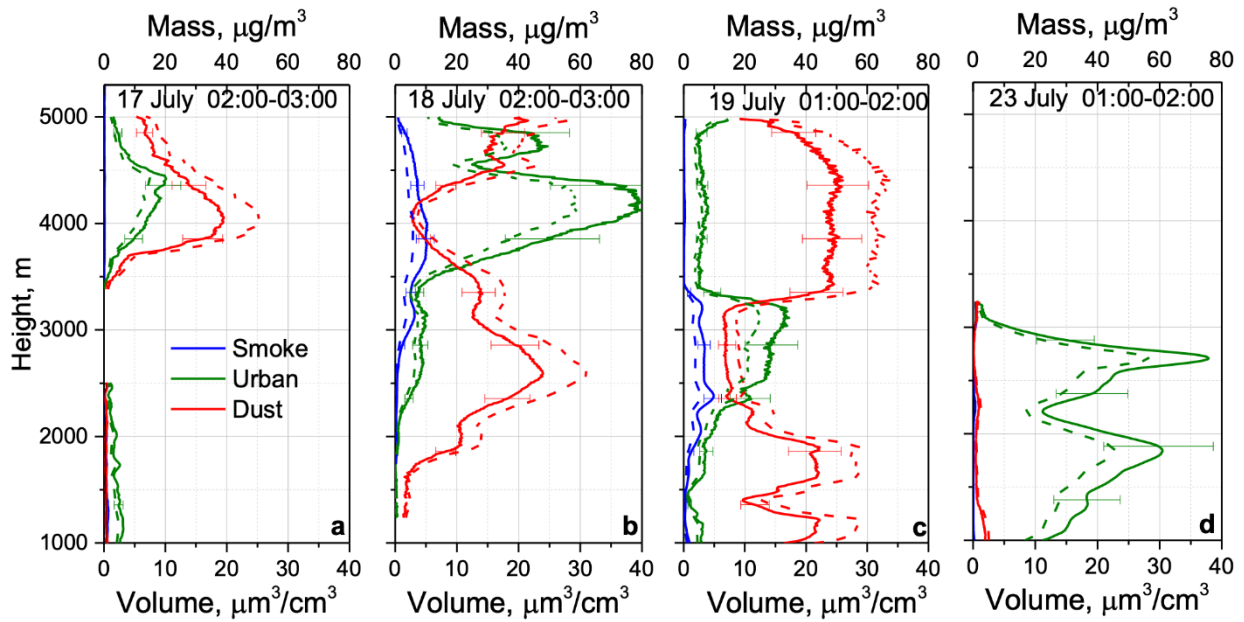
Fig.17. Vertical profiles of the volume concentration of smoke, dust and urban particles derived from η_s, η_u, and η_d presented in Fig.13, using the mean values of the lidar ratios and the conversion factors from Table 2. Profiles are shown for the episodes on (a) 17 July, (b) 18 July, (c) 19 July and (d) 23 July 2022. Dash lines depict the mass concentration calculated for the particle densities ρ_s=1.15 g/cm^3, ρ_u=1.5 g/cm^3, and ρ_d=2.6 g/cm^3.